




Interfacial electronic structure engineering on molybdenum sulfide for robust dual-pH hydrogen evolution

Mingqiang Liu^{1,2,7}, Jia-Ao Wang^{3,7}, Wantana Klysubun⁴, Gui-Gen Wang¹ [✉], Suchinda Sattayaporn⁴, Fei Li¹, Ya-Wei Cai¹, Fuchun Zhang⁵, Jie Yu¹ [✉] & Ya Yang^{1,2,6} [✉]

Molybdenum disulfide, as an electronic highly-adjustable catalysts material, tuning its electronic structure is crucial to enhance its intrinsic hydrogen evolution reaction (HER) activity. Nevertheless, there are yet huge challenges to the understanding and regulation of the surface electronic structure of molybdenum disulfide-based catalysts. Here we address these challenges by tuning its electronic structure of phase modulation synergistic with interfacial chemistry and defects from phosphorus or sulfur implantation, and we then successfully design and synthesize electrocatalysts with the multi-heterojunction interfaces (e.g., $1T_{0.81}\text{-MoS}_2\text{@Ni}_2\text{P}$), demonstrating superior HER activities and good stabilities with a small overpotentials of 38.9 and 95 mV at 10 mA/cm², a low Tafel slopes of 41 and 42 mV/dec in acidic as well as alkaline surroundings, outperforming commercial Pt/C catalyst and other reported Mo-based catalysts. Theoretical calculation verified that the incorporation of metallic-phase and intrinsic HER-active Ni-based materials into molybdenum disulfide could effectively regulate its electronic structure for making the bandgap narrower. Additionally, X-ray absorption spectroscopy indicate that reduced nickel possesses empty orbitals, which is helpful for additional H binding ability. All these factors can decrease Mo-H bond strength, greatly improving the HER catalytic activity of these materials.

¹Shenzhen Key Laboratory for Advanced Materials, School of Materials Science and Engineering, Harbin Institute of Technology, Shenzhen, People's Republic of China. ²CAS Center for Excellence in Nanoscience, Beijing Key laboratory of Micro-nano Energy and Sensor, Beijing Institute of Nanoenergy and Nanosystems, Chinese Academy of Science, Beijing, People's Republic of China. ³Department of Chemistry and the Oden Institute for Computational Engineering and Sciences, University of Texas at Austin, Austin, TX, USA. ⁴Synchrotron Light Research Institute, Muang, Nakhon Ratchasima, Thailand. ⁵School of Physics and Electronic Information, Yan'an University, Yan'an, People's Republic of China. ⁶School of Nanoscience and Technology, University of Chinese Academy of Sciences, Beijing, People's Republic of China. ⁷These authors contributed equally: Mingqiang Liu, Jia-Ao Wang.

✉email: wanguigen@hit.edu.cn; yayang@binn.cas.cn

Extensive use and depletion of fossil fuels resulting in serious pollution. Therefore, green and renewable fuel resources are required for continuing sustainable economic development^{1–3}. Electrocatalysis acts as a vital role in the conversion of clean energy to achieve a sustainable approach to various commercial processes, including HER^{4,5}. However, electrochemical water splitting is hindered by the large kinetic barrier and slow kinetics^{6–9}. Pt-based electrocatalysts are recognized as highly efficient electrocatalysts due to good electrical conductivity¹⁰, fast kinetics^{11,12}, and the preference to overcome the large kinetic energy barrier involved in the above-mentioned process¹³. Unfortunately, high price and not desirable stability hinder the extended Pt-based catalysts' application¹⁴. Thus, it is very urgent to develop cost-effective Pt-free electrocatalysts with comparable activity and better stability.

Researchers recently have designed a wide range of low-cost catalysts, including transition-metal chalcogenides (TMDCs)^{15,16}, metal nitrides^{17,18}, metal carbides^{19,20}, and metal phosphides^{21,22}. Among these candidates, MoS₂, a typical layered 2D TMDCs formed by Van der Waals interaction and stacking of S–Mo–S layers, attracts extensive interests with its adjustable bandgap, unique band structure, high energy-conversion efficiency, and earth abundance^{23–25}. However, the electrocatalytic activity of MoS₂ is closely associated with its surface electric structure^{26–36}, many researchers have focused on adjusting the electronic structure of the MoS₂ surface to promote electrocatalytic activity, such as surface engineering²⁶, doping²⁷, single-atom anchoring²⁸, phase structure^{29–33}, interface active site^{34,35}, and defect³⁶. Interestingly, two main phases of MoS₂ were widely justified: 2H and 1T phases²⁹. 2H phase has the most thermodynamical stability among the molybdenum sulfide family, whose HER activities are restrained by the amount and active site types as well as conductivity. Unlike the 2H phase, 1T-phase one demonstrates higher catalytic activity since it has numerous active sites on the edges and a fast transfer rate. However, it is remaining a giant challenge of directly synthesizing the high percentage 1T-phase molybdenum sulfide due to the thermodynamic instability of 1T_{phase}-MoS₂³⁰. To solve this problem, a feasible strategy is to efficiently realize the 2H → 1T-phase transformation to improve HER capability. Wang et al. found that a partial 2H → 1T-MoS₂ phase transition by facile one-pot annealing of a large amount of 2H_{phase}-MoS₂ under phosphorus vapor is able to enhance HER catalytic activities³¹. A synergistic strategy of doping nitrogen and intercalating PO₄^{3–} is reported, which can convert 2H- to 1T-phase with a conversion rate of up to 41%, and has excellent HER performance³². However, the electronic transport capacity and phase stability of the phase boundary of a single component (pure 1T-phase) are generally poor. In order to overcome the puzzles, the HER activity of the pure phase can be improved by constructing a heterogeneous boundary. Therefore, it is expected to further enhance the HER performance and its stability of traditional single 1T-phase or 2H-phase interface by constructing a composite heterojunction between 1T-phase and the other phases³³.

Interface modification could be an effective approach to construct a composite heterojunction^{34,35}. Ni-based materials (such as Ni₂P, NiS₂, Ni₂S₃, etc) with high activity and conductivity have been considered as highly efficient electrocatalysis materials for HER^{21,22,37}, as another heterogeneous interface, which is also very important to control the electronic structure of the MoS₂ interface. Kim et al. reported that Ni₂P nanoparticles were used to activate the MoS₂ base surface, which exhibits Pt-like HER performance in 0.5 M HCl solution³⁷. Because the electronic structure of Ni₂P is a *P62m* space group, which could facilitate recombination at the atomic scale. Moreover, Ni has a unique α and β orbital integral asymmetric *d* orbital, which makes it easy

for the lone pair of electrons to recombine with the *d* orbital of the exposed Mo atom on MoS₂ to generate new interface electrons, thereby improving HER performance. Lin et al. reported that a defect-rich heterogeneous interfacial catalyst (MoS₂/NiS₂) could provide abundant active sites to promote electron transfer, thereby further rapidly promoting electrocatalytic hydrogen evolution³⁸. More importantly, the introduction of NiS₂ hybridization on the surface of MoS₂ generates a new form of interface electrons, and Ni^{δ+} is reduced to low-valence Ni to improve the binding energy with hydrogen elements, thereby weakening the Mo–H strength. To sum up, although the heterojunction-phase catalyst synthesized by the above-mentioned approach further improves the HER activity and good stability, the understanding and regulation of the surface electronic structure on the MoS₂ interface are still huge challenges, and thus it is very necessary to develop an efficient synthesis approach to obtain stable multi-heterogeneous interface catalyst.

Here, we address these challenges by tuning its electronic structure through phase modulation synergistic with interfacial chemistry and defects of phosphorus or sulfur implantation, and we then successfully design and prepare a series of heterojunction-phase-interface electrocatalysts (denoted 1T_{0.81}-MoS₂@Ni₂P and 1T_{0.72}-MoS₂@NiS₂) with an outstanding HER activity and are stable in dual-pH surroundings. The strategies to control the electronic characteristics of the MoS₂ surface include surface phase modulation, surface defects, and the construction of hetero-structure (Fig. 1a). Furthermore, we control the hydrogen and hydroxyl adsorption energy through the synergistic effect of heterojunction-phase-interface catalysts (Fig. 1b, c–f) because the energy of the hydroxyl species is very important for the hydrolysis accelerator. Starting from hydrothermally synthesized MoS₂ nanosheets, we develop a simple surface electronic structure modulation strategy of constructing multi-heterogeneous-phase-interface 1T_{0.81}-MoS₂@Ni₂P and 1T_{0.72}-MoS₂@NiS₂ electrocatalysts (Fig. 1a) by citric acid-induced hydrothermal synthesis, electrodeposition and then phosphorus (or sulfur) vapor thermal treatment approach for the first time. Our approach can not only realize the construction of abundant catalytic reactive sites but also improve the conversion rate of 2H to 1T (81%), and it is also convenient to introduce Ni₂P or NiS₂ heterogeneous interfaces. As to the surface electronic structure of catalysts, high-resolution transmission electron microscopy (HRTEM) images show that such phase-structures, heterojunction-phase-interface edges, and defects are derived by the featured electronic states and Ni atomic coordination. Additionally, X-ray photoelectron spectra (XPS) showed that citric acid induces hydrothermal synthesis of stable 1T_{0.41}-MoS₂ (41% of 1T-phase), and the 1T_{0.81}-MoS₂ or 1T_{0.72}-MoS₂ (81% or 72% of 1T-phase) conversion rate is further improved after phosphorus or sulfur vapor thermal treatment. As-synthesized 1T_{0.81}-MoS₂@Ni₂P (or 1T_{0.72}-MoS₂@NiS₂) multi-heterogeneous catalyst exhibits the remarkable HER catalytic activity, achieving the low overpotentials of 38.9 (or 186) and 98.5 mV (or 128 mV) for HER at a current density of 10 mA/cm². They also have Tafel slopes of 41 (or 79) and 42 (or 68) mV/dec in 0.5 M H₂SO₄ or 1.0 M KOH media, and good stability during testing for 16 h in both media, respectively. The 1T_{0.81}-MoS₂@Ni₂P (or 1T_{0.72}-MoS₂@NiS₂) catalysts exhibited superior activities with Tafel slope values and the overpotentials lower than the values reported for Mo-base HER catalysts in both alkaline and acidic media^{30,31,33,37–40}. Moreover, as-synthesized 1T_{0.72}-MoS₂@NiS₂ (or 1T_{0.81}-MoS₂@Ni₂P) catalyst also exhibits excellent OER and overall-water splitting catalytic activity. DFT calculation results display that the introduction of 1T-phase MoS₂ and Ni-based materials can regulate MoS₂ electronic structure effectively for making the bandgap narrower, and decreasing H* and water adsorption energy. In situ electrochemical-Raman

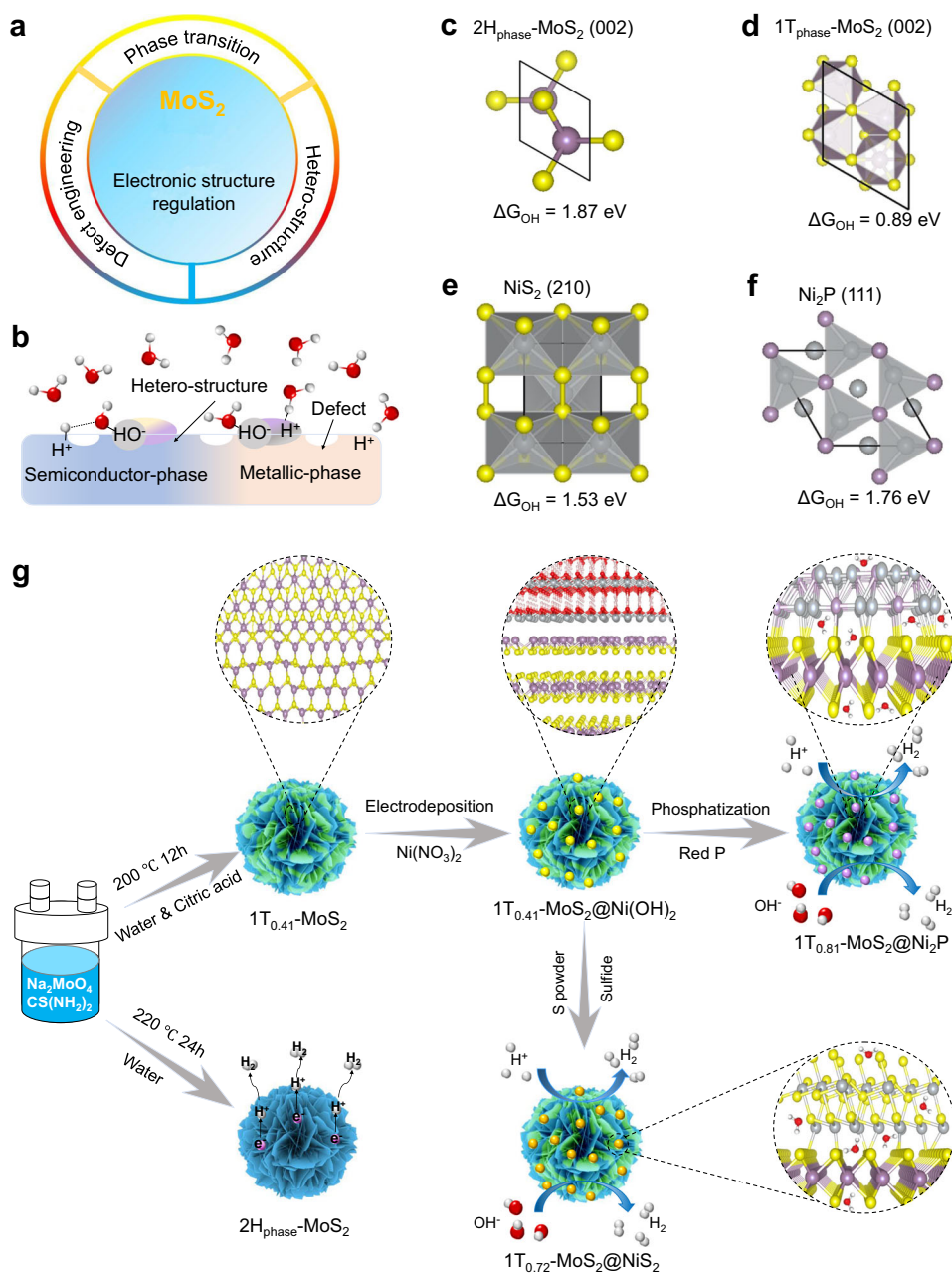


Fig. 1 Motivation and design of electrocatalyst. **a** Tuning strategy of the electronic structure of the MoS₂ surface. **b** Design ideas of hydrogen evolution catalyst. **c–f** the energetics of hydroxyl species on 2H_{phase}-MoS₂ (002), 1T_{phase}-MoS₂ (002), NiS₂ (210), and Ni₂P (111) HER electrocatalyst surfaces. **g** Schematics of the 1T_{0.72}-MoS₂@NiS₂ and 1T_{0.81}-MoS₂@Ni₂P synthesis steps.

spectra results indicate that the OH⁻ ions are driven to be adsorbed on Mo, Ni atoms in the alkaline medium, and then there forms the OOH* intermediates. There is a strong interaction between Ni and Mo on the surface of the catalyst, thereby increasing the local electronic state of Mo atoms, reducing the hydrogen-adsorption energy for protons on Mo atoms, and thus improving its intrinsic catalytic. Moreover, X-ray absorption spectroscopy results imply that reduced Ni supply empty *d*-orbitals to facilitate H atom capture, and decrease Mo–H strength of 1T_{0.81}-MoS₂@Ni₂P (or 1T_{0.72}-MoS₂@NiS₂) catalyst. This work provides useful insights for exploring the enhancement mechanisms of HER with an optimized surface electronic structure on the MoS₂ interface, which provides an effective insight of constructing invaluable metal electrocatalysts for HER and other fields.

Results

Preparation and characterizations of multi-heterojunction interface electrocatalysts. The formation process of multi-heterojunction interface electrocatalysts is schematically illustrated in Fig. 1g. 1T_{0.81}-MoS₂@Ni₂P and 1T_{0.72}-MoS₂@NiS₂ catalysts were synthesized by a three-step procedure. First, 1T_{0.41}-MoS₂ nanospheres were obtained on carbon cloth (CC) by acid-induced hydrothermal approach at 200 °C for 12 h (see details in “Methods” section). The as-obtained 1T_{0.41}-MoS₂ shows a large number of microspheres (Supplementary Fig. 1b–d) with a narrow diameter distribution of 2.0–4.0 μm distributed uniformly on the surface of CC substrate. Flower-shaped MoS₂ microspheres consist of many aligned 1T_{0.41}-MoS₂ nanosheets, on which the Ni(OH)₂ nanoparticles were then electrodeposited (see details in “Methods” section). 1T_{0.41}-MoS₂@Ni(OH)₂ material inherited its

morphology from spherical MoS₂. When being electrodeposited for 100 s, a small amount of Ni(OH)₂ nanoparticles can be anchored on the surface of MoS₂ nanospheres (Supplementary Fig. 2). As the electrodeposition time increases to 300 s, a large number of Ni(OH)₂ nanoparticles can be observed to adhere to the MoS₂ surface (Supplementary Fig. 3). Subsequently, as-prepared 1T_{0.41}-MoS₂@Ni(OH)₂ was loaded into a quartz tube mixed with red phosphorus or sulfur powder and sealed by oxyacetylene flame. Finally, these were heated to 600 °C for the reaction with red phosphorus or sulfur to synthesize 1T_{0.81}-MoS₂@Ni₂P and 1T_{0.72}-MoS₂@NiS₂ catalysts, respectively (Supplementary Figs. 4 and 5). As to 1T_{0.81}-MoS₂@Ni₂P catalyst, the MoS₂ microspheres are very rough, on which there distribute many random Ni₂P nanoparticles (Supplementary Fig. 5). It is because that the 1T/2H-mixed phase and heterojunction-interface structure reduces the adhesion of the gas-solid interface and facilitates releasing hydrogen from the catalyst surface, which is essential for enhancing HER³⁴.

Next, the phase composition and crystal structure of 1T_{0.81}-MoS₂@Ni₂P and 1T_{0.72}-MoS₂@NiS₂ were obtained by X-ray diffraction (XRD) and Raman spectroscopy. There are some obvious characteristic diffraction peaks of 14.3°, 33.4°, and 59.2° (Supplementary Fig. 6b, c), which can be ascribed to 2H_{phase}-MoS₂ (JCPDS#75-1539). However, the XRD peak of 1T_{0.81}-MoS₂@Ni₂P and 1T_{0.72}-MoS₂@NiS₂ located at 2θ ≈ 28.8° can be indexed as the (004) peak of 1T_{phase}-MoS₂, which indicates that 1T- and 2H-mixed phases were successfully hydrothermally synthesized⁴¹. The other characteristic peaks (2θ ≈ 31.3°, 35.2°, 38.8°, 44.9°, and 53.3°) demonstrate that the 1T_{0.72}-MoS₂@NiS₂ is a hybrid of NiS₂ (JCPDS#11-0099), which verifies the presence of NiS₂ nanoparticles. Similarly, as to 1T_{0.81}-MoS₂@Ni₂P catalyst, its XRD results also showed the presence of Ni₂P nanoparticles (JCPDS#21-0590) on the 1T_{0.41}-MoS₂ surface. Raman spectroscopy showed E_{2g}¹ and A_{1g} vibrational bands at 376.2 and 402.9 cm⁻¹ peaks typical for 2H_{phase}-MoS₂⁴². J₁, J₂, and J₃ vibrations at 147.3, 235.4 and 335.2 cm⁻¹ are characteristic for 1T_{phase}-MoS₂⁴³ (Supplementary Fig. 6b). These results prove that the 1T-phase of MoS₂ is formed by the hydrothermal reaction induced by organic acids (e.g., citric acid)⁴¹. 1T_{0.72}-MoS₂@NiS₂ or 1T_{0.81}-MoS₂@Ni₂P demonstrated three characteristic peaks of 1T_{phase}-MoS₂ and the two characteristic peaks (E_{2g}¹ and A_{1g}) of 2H_{phase}-MoS₂. Additionally, they showed a vibrational peak (437.3 cm⁻¹) of Ni-S³⁸ or three vibrational peaks (216.2, 249.7, and 269.5 cm⁻¹) of Ni-P³⁷. More importantly, the E_{2g}¹ and A_{1g} vibrations of 1T_{0.72}-MoS₂@NiS₂ at 382.2 and 408.1 cm⁻¹ were red-shifted by 6.0 and 5.2 cm⁻¹, respectively (Supplementary Fig. 6d). This could be attributed to the exploits the S layer of MoS₂ as an external S source to grow NiS₂ in situ. Therefore, it changes the original vibration mode of the Mo-S bonds, and the out-of-plane vibration mode has a more significant change⁴⁴⁻⁴⁶. Similarly, the E_{2g}¹ and A_{1g} peaks for the 1T_{0.81}-MoS₂@Ni₂P catalyst slightly red-shifted by 7.3 and 3.0 cm⁻¹, respectively, because of interfacial stress between Ni₂P and MoS₂, indicating that the formation of MoS₂@Ni₂P heterojunction leads to the Raman shift of MoS₂⁴⁴⁻⁴⁶. These results confirm that rich multi-heterojunction interface edges active sites catalysts were successfully synthesized.

Electronic structure characterizations of 1T_{0.72}-MoS₂@NiS₂ and 1T_{0.81}-MoS₂@Ni₂P catalysts. To further identify the surface electronic structure of multi-heterogeneous interface catalysts, we applied the high-resolution transmission electron microscopy (HRTEM) to assess the morphology and crystal structures of 1T_{0.81}-MoS₂@Ni₂P and 1T_{0.72}-MoS₂@NiS₂ catalysts. Supplementary Fig. 7a, b shows the typical low-magnification image of

the 1T_{0.72}-MoS₂@NiS₂ on the Cu grid, which confirms the flower-like nanosphere morphologies of 1T_{0.72}-MoS₂@NiS₂. TEM and corresponding elemental distribution map obtained for the 1T_{0.72}-MoS₂@NiS₂ sample demonstrated uniformly distributed Mo, Ni, and S (Supplementary Fig. 7c-c4). As revealed by the HRTEM image (Fig. 2a-c and Supplementary Fig. 7e, f), NiS₂ nanoparticles are decorated on MoS₂ nanosheets edge (Supplementary Fig. 10a, b). The HRTEM image of 1T_{0.72}-MoS₂@NiS₂ clearly shows the crystal lattice of 0.25 nm, referring to the NiS₂ (210). Interestingly, Fig. 2a shows the HRTEM image of 1T_{0.72}-MoS₂@NiS₂ flower-like nanosheets, which there demonstrate the lattice fringes perpendicularly to the electron beam direction circled by blood color, justifying the S defect (Fig. 2c). The trigonal lattice in the yellow circle implies the presence of 1T-phase MoS₂, while the hexagonal lattice in the blue circle suggests the presence of 2H phase MoS₂. The above-described results further confirm the successful preparation of the 1T_{0.72}-MoS₂@NiS₂ multi-heterojunction interface catalyst. The anion is changed to be P to produce 1T_{0.81}-MoS₂@Ni₂P multi-heterojunction interface catalyst by phosphorus vapor thermal treatment. Supplementary Fig. 8a, b displays the morphologies of 1T_{0.81}-MoS₂@Ni₂P catalyst, overlapping nanosheets with many embedded particles can be clearly identified. There is an obvious alternation of 1T and 2H phases, and a large number of defects or disorder (Fig. 2f and Supplementary Fig. 9). As shown in Supplementary Fig. 8c, there are the distributions of Mo, Ni, S, and P over the whole 1T_{0.81}-MoS₂@Ni₂P, verifying that Ni₂P nanoparticles are encapsulated by MoS₂ edges (Supplementary Fig. 10c, d). The interplanar spacings of 0.62 and 0.22 nm are assigned to (002) and (111) interplanar distances of MoS₂ and Ni₂P, respectively (Fig. 2d, e). Similarly, Fig. 2e, f displays two amplified HRTEM images truncated from Fig. 2d, in which Fig. 2f demonstrates some hexagonal and trigonal lattice areas of semiconductor 2H_{phase}- and metallic 1T_{phase}-MoS₂, respectively. The HRTEM results further confirm the successful preparation of the 1T_{0.81}-MoS₂@Ni₂P multi-heterojunction interface catalyst.

Next, we performed XPS measurement to assess the elemental valence states of all the as-synthesized samples (Fig. 2g-i and Supplementary Fig. 13a). Full XPS spectrum for 1T_{0.72}-MoS₂@NiS₂ (Supplementary Fig. 13a) showed that atomic ratios of Mo, S, and Ni were equal to 13.96%, 36.96%, and 4.39%, respectively, and close to that measured by HRTEM elemental mapping (~14.30%, 35.87%, and 4.76%). Mo 3d spectra obtained for the 1T_{0.41}-MoS₂ sample shows Mo⁴⁺ 3d_{3/2} and Mo⁴⁺ 3d_{5/2} peaks at 232.68 and 229.43 eV (Fig. 2g), respectively, confirming the existence of Mo⁴⁺ for the 1T_{0.41}-MoS₂. As to the 1T_{0.72}-MoS₂@NiS₂, or 1T_{0.81}-MoS₂@Ni₂P heterostructures catalyst, the high-resolution Mo 3d XPS spectrum shows that both Mo⁴⁺ 3d_{3/2} and Mo⁴⁺ 3d_{5/2} peaks for mixed-phase MoS₂ has a shift of 0.23 eV and 0.15 eV to lower binding energy compared with 1T_{0.41}-MoS₂ (Supplementary Fig. 11a), which is attributed to the existence of 1T_{phase}-MoS₂⁴⁷. In addition, two peaks of 163.41 and 162.22 eV are observed in the 1T_{0.41}-MoS₂, corresponding to S²⁻ 2p_{1/2} and S²⁻ 2p_{3/2}, respectively (Fig. 2h). However, the binding energies of S²⁻ 2p_{1/2} and S²⁻ 2p_{3/2} in 1T_{0.72}-MoS₂@NiS₂, or 1T_{0.81}-MoS₂@Ni₂P heterostructures catalyst shift to 163.28 and 162.10 eV, respectively (Supplementary Fig. 11b). This negative-shift (0.13 eV) suggests little electron transfer between NiS₂ (or Ni₂P) and MoS₂, also suggesting the reconfiguration of the electronic structure during the transferring of electron from Mo⁴⁺ to the surrounding Ni sites⁴⁸. Interestingly, the 1T-phase contents in the 1T_{0.81}-MoS₂@Ni₂P and 1T_{0.72}-MoS₂@NiS₂ samples (81% and 72%, respectively) were higher than the 41% value observed for the 1T_{0.41}-MoS₂. Thus, phosphorus or sulfur implantation further facilitates the phase transformation of 1T_{phase}-MoS₂^{24,32}. The reason may be that phosphorus can be

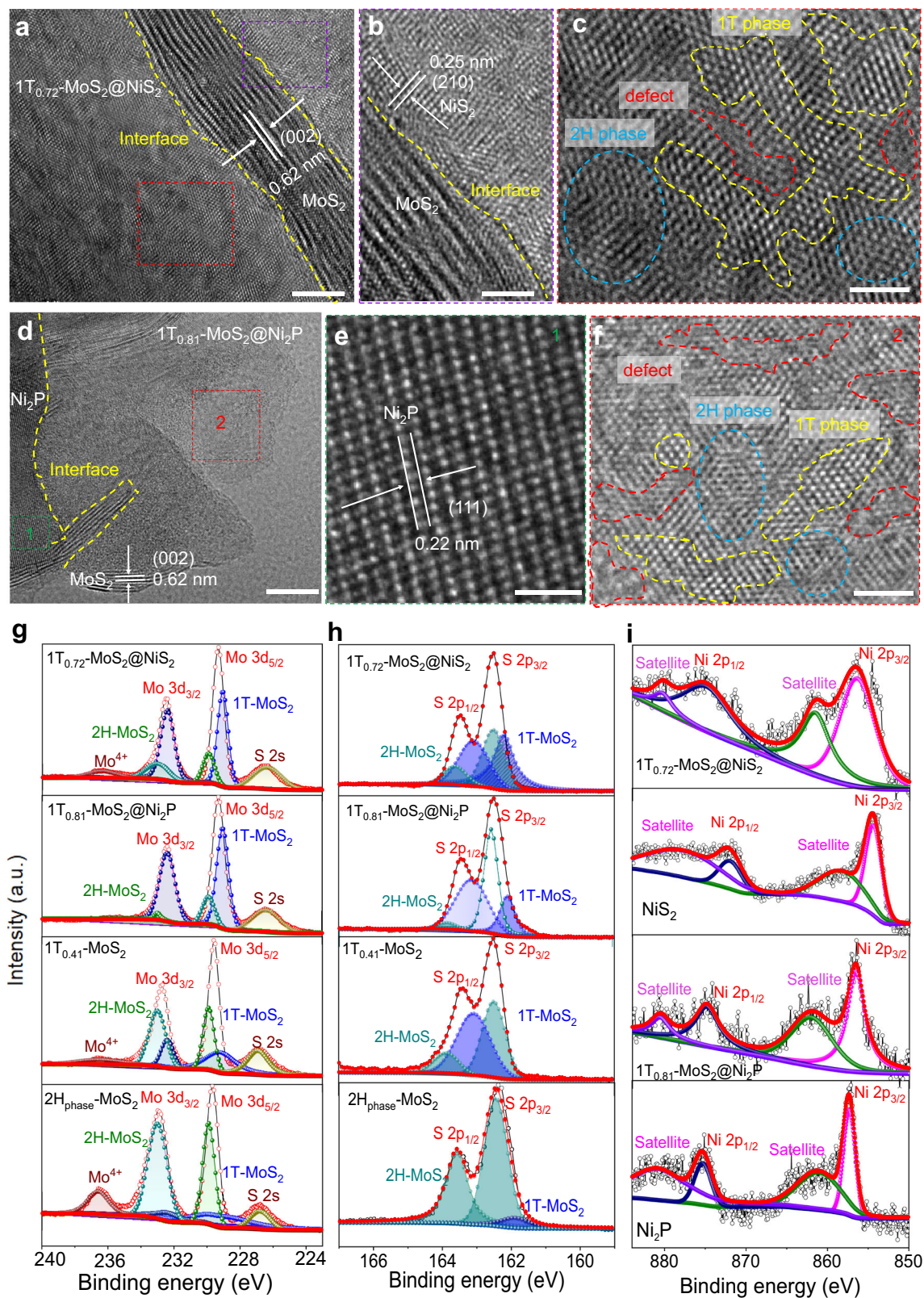


Fig. 2 Electronic structure characterizations of 1T_{0.72}-MoS₂@NiS₂ and 1T_{0.81}-MoS₂@Ni₂P catalysts. a-c HRTEM image of 1T_{0.72}-MoS₂@NiS₂. **a** MoS₂ lattice, scale bars are 5 nm. **b** NiS₂ lattice and heterojunction interface, scale bars are 1 nm. **c** shows 2H and 1T lattices, scale bars are 2 nm. **d-f** Typical HRTEM image of 1T_{0.81}-MoS₂@Ni₂P. **d** shows MoS₂ lattice and heterojunction interface, scale bars are 5 nm. **e** shows Ni₂P lattice fringes, scale bars are 1 nm. **f** shows 2H and 1T lattices, scale bars are 2 nm. **g** HR Mo 3d core-level XPS spectra of 1T_{0.72}-MoS₂@NiS₂, 1T_{0.81}-MoS₂@Ni₂P, 1T_{0.41}-MoS₂, and 2H_{phase}-MoS₂. **h** S 2p core-level XPS spectra of 1T_{0.72}-MoS₂@NiS₂, 1T_{0.81}-MoS₂@Ni₂P, 1T_{0.41}-MoS₂ and 2H_{phase}-MoS₂, respectively. **i** Ni 2p XPS spectrum for 1T_{0.72}-MoS₂@NiS₂, 1T_{0.81}-MoS₂@Ni₂P, pure Ni₂P, and Ni₂S.

simultaneously inserted into S–Mo–S atomic planes, inducing the glide of S atomic planes, affording in-plane heterostructures between 1T and 2H MoS₂ domains (Supplementary Fig. 14), which is consistent with previous reports^{31,32}. As shown in Fig. 2i, the Ni 2*p* spectrum of 1T_{0.81}-MoS₂@Ni₂P shows two spin–orbit doublets at 856.6 and 874.9 eV corresponding to Ni²⁺ 2*p*_{3/2} and Ni²⁺ 2*p*_{1/2} oxidation states in Ni₂P, respectively, and two satellite peaks (identified as “Satellite.”)⁴⁹. Notably, compared with the binding energies of Ni 2*p*_{3/2} (857.4 eV) and Ni 2*p*_{1/2} (875.4 eV) of pure Ni₂P, the two binding energies of Ni 2*p*_{3/2} and Ni 2*p*_{1/2} have a significant negative-shift of approximately 0.8 and 0.6 eV in 1T_{0.81}-MoS₂@Ni₂P (Fig. 2i), respectively. This result implies the transfer of electrons from Mo⁴⁺ to Ni²⁺ sites in the 1T_{0.81}-MoS₂@Ni₂P sample, resulting in a low-valence state and electron-rich structure of Ni²⁺ sites⁵⁰. For pure NiS₂ sample, the peaks of Ni 2*p*_{3/2} and Ni 2*p*_{1/2} located at 854.7 and 872.2 eV, and the corresponding satellites appear at 858.7 and 878.6 eV, respectively. However, the binding energies of Ni 2*p*_{3/2}, Ni 2*p*_{1/2} and satellite in 1T_{0.72}-MoS₂@NiS₂ sample (Fig. 2i) are positive-shifted to 856.6 (by 1.9 eV), 875.3 (by 3.1 eV), 861.8 (by 3.1 eV) and 862.2 eV (by 1.9 eV), respectively. The positive-shift of the Ni 2*p* binding energies peaks manifest a higher valence state, which are ascribed to Ni bonded to S and O atoms, such as sulfides or surface oxides/hydroxides⁵¹. For the 1T_{0.81}-MoS₂@Ni₂P, the P 2*p* spectrum shows two peaks at 130.4 and 129.5 eV corresponding to P 2*p*_{1/2} and P 2*p*_{3/2}, respectively, suggesting the existence of Ni₂P. In addition, it also can be observed another peak at 134.7 eV of oxidized phosphate (P–O) species (Supplementary Fig. 13b), which is due to the partial oxidation of Ni₂P in air. Notably, the binding energies of Ni 2*p*_{3/2} (852.7 eV) and P 2*p*_{3/2} (129.5 eV) are both shifted, indicating that charge transfer occurs from Ni to P, which can greatly promote the catalytic activity of 1T_{0.81}-MoS₂@Ni₂P.

Electrocatalytic HER performances in alkaline and acidic media.

1T_{0.72}-MoS₂@NiS₂ and 1T_{0.81}-MoS₂@Ni₂P electrodes exhibited attractive multi-heterogeneous interface edges, plentiful active sites, and abundant mass transfer and gas release channels and are expected to be used as very effective and stable catalysts for H₂ production. First, we analyzed HER activities (in 1.0 M KOH) of the electrodes containing these electrodes. The 1T_{0.72}-MoS₂@NiS₂ and 1T_{0.81}-MoS₂@Ni₂P electrodes exhibit small overpotentials of 95 and 170 mV at 10 mA/cm², respectively (see linear sweep voltammetry (LSV) results in Fig. 3a), which are better than the commercial Pt/C electrode (127 mV). To in-depth understand the HER kinetic mechanism, we calculated the Tafel slopes of these electrodes using the Tafel equation⁵² and obtained the smallest slopes equal to 68 and 79 mV/dec for the 1T_{0.72}-MoS₂@NiS₂ and 1T_{0.81}-MoS₂@Ni₂P electrodes, respectively (Supplementary Fig. 15a). These values are even closer to the Tafel slope of the Pt/C electrode (56 mV/dec). Thus, the 1T_{0.72}-MoS₂@NiS₂ and 1T_{0.81}-MoS₂@Ni₂P electrodes as active electrocatalysts exhibit the fastest HER processes and better reactivity, which is attributed to the multi-heterogeneous interface effect, a large number of defects, and a higher proportion of 1T_{phase}-MoS₂. Next, we evaluated the long-term cycling stability of the as-prepared electrodes using the chronopotentiometry technique at 10 and 30 mA/cm², respectively. The 1T_{0.72}-MoS₂@NiS₂ and 1T_{0.81}-MoS₂@Ni₂P electrodes were very robust and exhibited negligible damping after 16 h measurement (Supplementary Fig. 15b), and the LSV curves measured before and after the long-term tests are almost the same (Supplementary Fig. 15c), demonstrating excellent long-term stability. Supplementary Fig. 15d lists the overpotential values for the 20.0 wt % Pt/C, 1T_{0.72}-MoS₂@NiS₂, and 1T_{0.81}-MoS₂@Ni₂P electrodes in 1.0 M

KOH at various current densities. 1T_{0.72}-MoS₂@NiS₂ electrodes exhibited lower overpotential. Generally, low overpotential and Tafel slope values demonstrated the superior HER catalytic activities, which was the case for our 1T_{0.72}-MoS₂@NiS₂ and 1T_{0.81}-MoS₂@Ni₂P electrodes. Moreover, 1T_{0.72}-MoS₂@NiS₂ electrode has such excellent HER activity comparable to those of as-reported Mo-based materials (Fig. 3b) and composites and various representative catalysts^{30,31,33,37–40} (Supplementary Table 3). Thus, 1T_{0.72}-MoS₂@NiS₂ electrode is a catalyst with the best HER activity in alkaline solutions.

To obtain the electrochemically active area (ECSA) of the 1T_{0.72}-MoS₂@NiS₂ and 1T_{0.81}-MoS₂@Ni₂P electrodes, the double-layer capacitance (*C*_{dl}) was calculated because the two values are proportional to each other. Therefore, we tested their cyclic voltammetry (CV) by continuously increasing scanning speed (Supplementary Fig. 16a–c) in order to obtain the CV curve of the electrode materials in the non-Faraday region (–0.2 to 0.4 V). Then, as shown in Supplementary Fig. 16d, the *C*_{dl} was calculated from the plot slope (slope = 2*C*_{dl}) between current-density difference (Δj) (0.15 V vs. RHE) and scan rate. The 1T_{0.72}-MoS₂@NiS₂ electrodes possessed the highest *C*_{dl} value (*C*_{dl} = 359.7 mF/cm²), suggesting a multi-heterogeneous interface could be effectively enhanced conductivity and exposed more active sites of as-prepared electrodes. We recorded the electrochemical impedance spectra (EIS). The corresponding Nyquist (Supplementary Fig. 17) of the 1T_{0.72}-MoS₂@NiS₂ electrode showed the lowest value for the charge transfer resistance (*R*_{ct}). Thus, it possessed very favorable charge transfer kinetics. To further reveal the intrinsic catalytic activity of each active sites, the turnover frequency (TOF) is also calculated⁵³. Based on the above-mentioned analysis, CV approach is regarded as the promising way to determine reasonable results (Supplementary Fig. 18). The TOF value of 1T_{0.81}-MoS₂@Ni₂P (3.56 S^{–1}) and 1T_{0.72}-MoS₂@NiS₂ (2.26 S^{–1}) heterojunction catalyst at the overpotential of 200 mV is 18.7 and 11.9 times higher than of 2H_{phase}-MoS₂ catalyst (0.19 S^{–1}) for HER, respectively (Supplementary Table 1). Typically, the amount of hydrogen evolution was measured of 1T_{0.72}-MoS₂@NiS₂ catalyst in 1.0 M KOH solution (Supplementary Fig. 19), presenting HER Faraday efficiency of 97.6 ± 0.6%, owing to the synergistic effect of the phase, defect and interface engineering of electrocatalyst.

Next, we also studied the HER performance of all the as-prepared electrodes in 0.5 M H₂SO₄ (Fig. 3c). The HER catalytic performance of the 1T_{0.81}-MoS₂@Ni₂P and 1T_{0.72}-MoS₂@NiS₂ electrodes was significantly improved their HER activities according to the LSV data: their overpotential values at 10 mA/cm² were as low as 38.5 and 152 mV, respectively, which is lower than the values for the electrodes containing 1T_{0.41}-MoS₂-Ni(OH)₂ (236 mV), 1T_{0.41}-MoS₂ (389 mV), 1T_{phase}-MoS₂ (392 mV), and 2H_{phase}-MoS₂ (354 mV). The Tafel slopes for the 1T_{0.81}-MoS₂@Ni₂P and 1T_{0.72}-MoS₂@NiS₂ electrodes were 41 and 42 mV/dec (Supplementary Fig. 20a). These values were lower than the values obtained for 1T_{0.41}-MoS₂ (169 mV/dec), 1T_{phase}-MoS₂ (163 mV/dec), and 2H_{phase}-MoS₂ (189 mV/dec) electrodes and were better than the electrode based on 20 wt% Pt/C (86 mV/dec). It is probably because, in the acidic environment, the H₂ desorption is the limiting step because H⁺ are abundant. The 1T_{0.81}-MoS₂@Ni₂P electrode had a weaker adsorption capacity toward H_{ads} so it exhibits a better catalytic effect than 2H_{phase}-MoS₂⁵⁴. Meanwhile, compared to the other electrodes, 1T_{0.81}-MoS₂@Ni₂P also has a higher ECSA because it has a larger *C*_{dl} (*C*_{dl} = 106.15 mF/cm², Supplementary Fig. 21) and, as a result, more catalytic sites, which significantly contributed to the overall activity. Furthermore, 1T_{0.81}-MoS₂@Ni₂P also possesses a much smaller *R*_{ct}, in contrast to other electrodes at 300 mV overpotential vs. RHE (Supplementary Fig. 22), revealing

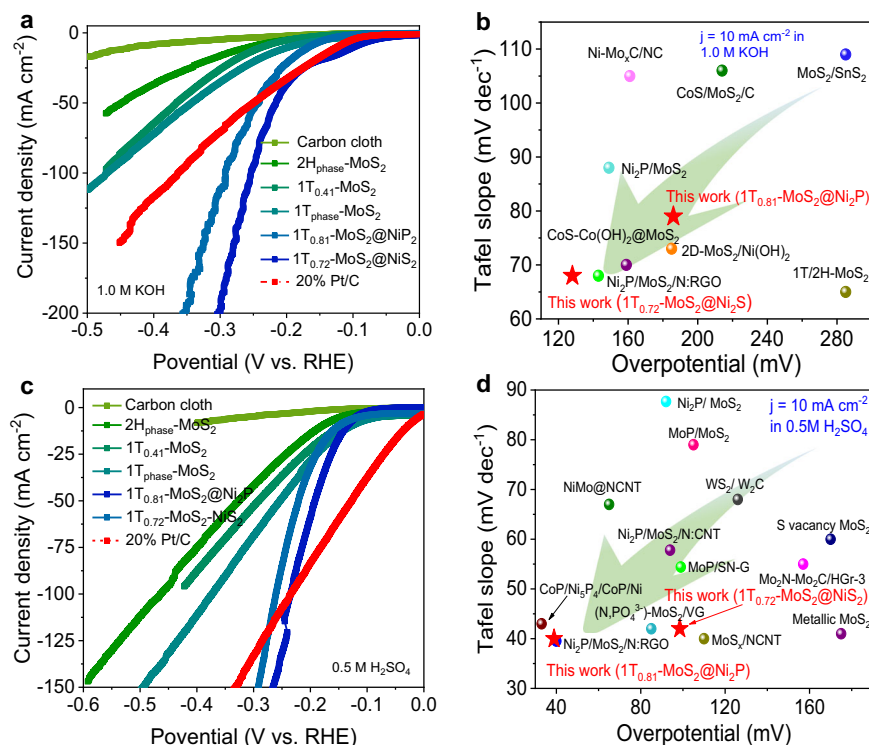


Fig. 3 HER was performed in alkaline and acidic electrolytes. **a** LSV curves in 1 M KOH. **b** η_{10} and Tafel slopes for various Mo-based HER electrocatalysts in 1.0 M KOH. **c** LSV curves in 0.5 M H₂SO₄. **d** η_{10} and Tafel slopes for various Mo-based HER catalysts in 0.5 M H₂SO₄. (All LSV curves were corrected without iR-compensation).

satisfied electron transport and good catalytic kinetics, which leads to high activity and low Tafel slope. Supplementary Fig. 20b shows that at 10 and 45 mA/cm², 1T_{0.81}-MoS₂@Ni₂P and 1T_{0.72}-MoS₂@NiS₂ electrodes were very durable and possesses negligible damping after 16 h measurement, which displays excellent long-term stability. In addition, even after 16 h of a chronoamperometric stability test of the electrodes, the current density remains above 95% (Supplementary Fig. 20c), and there is only a slight deviation for the LSV recorded after the stability test, indicating that as-prepared electrodes have very good stability in an acidic environment. As to 20.0 wt% Pt/C, 1T_{0.72}-MoS₂@NiS₂, and 1T_{0.81}-MoS₂@Ni₂P electrodes in 0.5 M H₂SO₄, Supplementary Fig. 20d shows overpotentials vs. various current densities. 1T_{0.81}-MoS₂@Ni₂P exhibits lower overpotential. We also compared the overpotentials (at 10 mA/cm² in acidic medium) and Tafel slopes with previously excellent Mo-based electrocatalysts^{8,32,37,55–57} (Fig. 3d and Supplementary Table 4). Catalytic HER performance of 1T_{0.81}-MoS₂@Ni₂P is also superior. Afterward, the amount of hydrogen evolution of 1T_{0.81}-MoS₂@Ni₂P catalyst was given in Supplementary Fig. 23, demonstrating a promising Faraday efficiency of 98.7 ± 0.5% towards real water splitting into hydrogen. Based on the above-mentioned results, 1T_{0.81}-MoS₂@Ni₂P multi-heterogeneous interface catalyst shows the remarkable intrinsic HER activities in acidic medium mainly attributed to multi-heterointerface interface edges active sites. In addition, as-synthesized 1T_{0.72}-MoS₂@NiS₂ (or 1T_{0.81}-MoS₂@Ni₂P) catalyst also exhibits excellent OER and overall-water splitting catalytic activity (Please see Supplementary Information for details, Supplementary Figs. 25–27).

Theoretical calculation and mechanisms analysis of the surface electronic structure and HER activation energy for the as-prepared electrocatalysts. To explain the distinguished

synergistic effect of 1T_{0.72}-MoS₂@NiS₂ (or 1T_{0.81}-MoS₂@Ni₂P) multi-heterogeneous interface catalysts, Density functional theory (DFT) calculations were also performed. Model building and computational parameters can be seen in the “Methods” section. Firstly, the interfacial electron interaction was investigated. The charge difference images (Fig. 4a, b and Supplementary Fig. 37) reveal the charge transfer from 1T_{0.41}-MoS₂ to the Ni₂S or/and Ni₂P interface, and the introduction of 1T-phase is more conducive to charge transfer from MoS₂ to NiS₂ or Ni₂P interface, which significantly increases the interface electron concentration and thus improves its activity. To better understand the surface electronic structure reconfiguration of MoS₂ through a coordinated phase transition and interface regulation in theory, the band structure and density of states (DOS) of bare NiS₂, Ni₂P, 2H_{phase}-MoS₂, 1T_{phase}-MoS₂, 2H_{phase}-MoS₂@NiS₂, 2H_{phase}-MoS₂@Ni₂P, 1T_{phase}-MoS₂@NiS₂, and 1T_{phase}-MoS₂@Ni₂P (Fig. 4c–e and Supplementary Figs. 38–40) obtained using the hybrid DFT–HSE06 exchange–correlation functional, which is presented in the Supplementary Information. The calculation results show that the bare NiS₂ exhibits typical semiconductor characteristics (Fig. 4c), with a narrow bandgap equal to 0.68 eV (Supplementary Figs. 38 and 39a). The band structure of 1T_{phase}-MoS₂ (Fig. 4d) and 1T_{phase}-MoS₂@NiS₂ (Fig. 4e) exhibited a certain zero bandgap, indicating a complete transition from the semiconductor phase (0.91 eV) to the metallic phase (0 eV) with improved conductivities²⁷. Notably, the intensity of PDOS of 1T_{phase}-MoS₂@NiS₂ was higher than that of 1T_{phase}-MoS₂ and NiS₂ at the Fermi level (Supplementary Figs. 38 and 39). Thus, the electron mobility of the 1T_{phase}-MoS₂@NiS₂ catalysts was more favorable for the efficient charge transfer, which agrees consistent with the EIS test results⁵⁸. Moreover, the PDOS results imply that the NiS₂ interface hybrid generates some new interface electronic states in 1T_{phase}-MoS₂ (Supplementary Fig. 39c), which was very likely because of the hybridization of the *d*-orbital of Mo

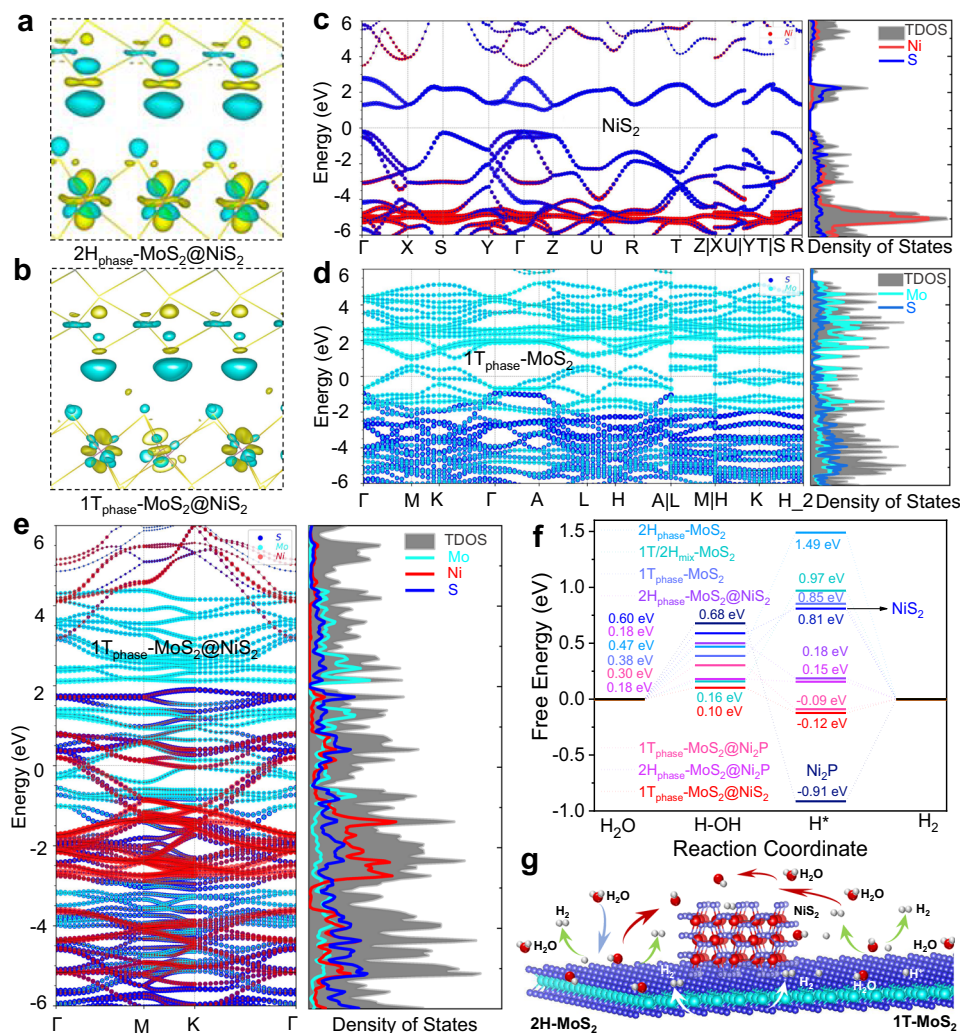


Fig. 4 Theoretical calculation and mechanisms analysis of the surface structure and HER activation energy of the as-prepared electrocatalysts. the deformation of the electronic density of **a** $2H_{\text{phase}}\text{-MoS}_2\text{@NiS}_2$ and **b** $1T_{\text{phase}}\text{-MoS}_2\text{@NiS}_2$ interface, in which yellow/green isosurfaces correspond to positive/negative spin densities ($0.00295308 \text{ e}/\text{\AA}^3$). Band structure and density of states (DOS) for **c** NiS_2 , **d** $1T_{\text{phase}}\text{-MoS}_2$ and **e** $1T_{\text{phase}}\text{-MoS}_2\text{@NiS}_2$. **f** Free-energy diagrams for HER on the $2H_{\text{phase}}\text{-MoS}_2$, $1T_{\text{phase}}\text{-MoS}_2$, pure Ni_2P , pure NiS_2 , $1T/2H_{\text{mix}}\text{-MoS}_2$, $2H_{\text{phase}}\text{-MoS}_2\text{@Ni}_2\text{P}$, $2H_{\text{phase}}\text{-MoS}_2\text{@NiS}_2$, $1T_{\text{phase}}\text{-MoS}_2\text{@NiS}_2$ and $1T_{\text{phase}}\text{-MoS}_2\text{@Ni}_2\text{P}$ interface edge. **g** Schematics showing water activation, *H intermediate formation and hydrogen generation on multi-heterojunction electrocatalysts.

and an empty *d*-orbital of Ni. Thus, higher HER activity of $1T_{\text{phase}}\text{-MoS}_2\text{@NiS}_2$ in comparison to $1T_{\text{phase}}\text{-MoS}_2$ agrees with the Fermi level DOS (Fig. 4d, e). Thus, the actual electrochemical performance would show even faster conductivity and charge transfer kinetics.

To reveal further the relationship of HER activity of catalysts with phase structure and heterojunction-interface, we used DFT to calculate the optimized structures and free-energy diagrams for HER on $2H_{\text{phase}}\text{-MoS}_2$, $1T_{\text{phase}}\text{-MoS}_2$, $1T/2H_{\text{mix}}\text{-MoS}_2$, pure Ni_2P , pure NiS_2 , $2H_{\text{phase}}\text{-MoS}_2\text{@NiS}_2$, $2H_{\text{phase}}\text{-MoS}_2\text{@Ni}_2\text{P}$, $1T_{\text{phase}}\text{-MoS}_2\text{@NiS}_2$, and $1T_{\text{phase}}\text{-MoS}_2\text{@Ni}_2\text{P}$ catalysts with partially multi-heterojunction interface modification. As shown in Fig. 4f and Supplementary Fig. 42, the reaction pathway for alkaline HER is constructed^{59,60}, including prior H_2O dissociation to form H^* intermediates (Volmer step) and hydrogen generation (Tafel step or Heyrovsky step). However, the energy of the intermediate state H^* (ΔG_{H^*}) is a critical indicator of the ability of hydrogen evolution (Tafel step or Heyrovsky step)^{35,59}. Figure 4f displays the calculated free-energy diagram on the most stable energy of the $2H_{\text{phase}}\text{-MoS}_2$, $1T_{\text{phase}}\text{-MoS}_2$, Ni_2P , NiS_2 , $2H_{\text{phase}}\text{-MoS}_2\text{@Ni}_2\text{P}$, $2H_{\text{phase}}\text{-MoS}_2\text{@NiS}_2$, $1T_{\text{phase}}\text{-MoS}_2\text{@NiS}_2$,

and $1T_{\text{phase}}\text{-MoS}_2\text{@Ni}_2\text{P}$ catalysts (Supplementary Fig. 41). For $2H_{\text{phase}}\text{-MoS}_2$, the ΔG_{H^*} is very positive (1.49 eV), indicating that there is a strong interaction between H^* and $2H_{\text{phase}}\text{-MoS}_2$, showing poor HER reaction kinetics. More importantly, MoS_2 shows unfavorable catalyst-OH_{ad} energetics ($\Delta G_{\text{H}_2\text{O}} = 0.82 \text{ eV}$), suggesting that the relatively high activated H_2O -adsorption energy will hinder the decomposition of H_2O into H^* intermediates and results in slow HER kinetics. The introduction of the $1T/2H_{\text{mix}}$ -phase into MoS_2 can obviously decrease the value of ΔG_{H^*} to 0.97 eV and $\Delta G_{\text{H}_2\text{O}}$ to 0.16 eV, implying promoted HER activity compared to $2H_{\text{phase}}\text{-MoS}_2$. Notably, constructing multi-heterointerface interface edges active sites with NiS_2 can provide the active sites for $-\text{OH}$ adsorption, and the followed $\Delta G_{\text{H}_2\text{O}}$ and ΔG_{H^*} are decreased to 0.10 and -0.12 eV on the $1T_{\text{phase}}\text{-MoS}_2\text{@NiS}_2$ interface, indicating the $1T/2H_{\text{mix}}$ -phase and NiS_2 nanoparticles are effective for cleaving HO-H bonds and weaker interaction between H^* . Also, the charge transfer from Ni_2P to the MoS_2 is verified by the DFT calculations, and hence there is a more optimal ΔG_{H^*} value of about -0.09 eV . Hence, the NiS_2 (or Ni_2P) can act as a promoter of H_2O dissociation and form hydrogen intermediates which then

adsorb on nearby MoS₂ catalyst sites. In this way, the multi-heterointerface can also accelerate the subsequent generation of H₂. The reaction pathways on the single side (such as Ni₂P, NiS₂, and MoS₂) of the interface have also been shown in Fig. 4f and Supplementary Fig. 42. These both show there is more unfavorable energetics than that of the synergetic pathway on MoS₂@NiS₂ or MoS₂@Ni₂P interface. The reason is that H* adsorbed on the surface of 2H_{phase}-MoS₂ binds to Mo atoms, and strong Mo–H strength and poor conductivity. However, H* can be absorbed not only by the 1T_{phase}-MoS₂@NiS₂ surface. Ni atoms possess empty *d* orbitals capable of binding H atoms, thereby weakening the Mo–H strength. More importantly, the introduction of the 1T-phase not only increases its electrical conductivity but also creates abundant active sites at the multi-heterojunction interface edges, which synergistically promote HER activity (Fig. 4g). Thus, our work demonstrates a novel and efficient design to create multi-heterogeneous interfacial electrocatalysts without noble metal materials and with excellent HER activity.

In situ electrochemical-Raman spectroscopy. To better understand the active sites of the 1T_{0.81}-MoS₂@Ni₂P and 1T_{0.72}-MoS₂@NiS₂ electrodes during the HER process, we used in situ Raman spectroscopy to study it (Supplementary Fig. 46). The in situ Raman test system is shown in Supplementary Fig. 46a. The as-prepared sample, Ag/AgCl, and Pt wires were used as working electrode, reference electrode, and counter electrode, respectively. In addition, the electrolyte was 1.0 M KOH. As shown in Supplementary Fig. 46c, d, the Raman spectra of 1T_{0.72}-MoS₂@NiS₂ electrode collected under potentiostatic conditions at stepped potential values from 0 V to –1.5 V. The results show that three characteristic peaks (147.3, 235.4, and 335.2 cm⁻¹ are attributed to J₁, J₂, and J₃ vibrations) of 1T-MoS₂, two characteristic peaks (382 and 407 cm⁻¹ are attributed to the E_{2g}¹ and A_{1g} vibrational bands) of 2H-MoS₂, and a vibrational peak (437.3 cm⁻¹) of Ni–S. However, when the 1T_{0.72}-MoS₂@NiS₂ sample was put in the electrolyte solution (1.0 M KOH solution), at different applied voltages from the –0.4 to –1.5 V during electrocatalytic HER, these Raman peaks are significantly enhanced. In addition, many new peaks aroused at 152, 188, 222, 284, 322, 453, 500, 548 cm⁻¹ of MoS₂, respectively⁶¹. The changes of these Raman peaks indicate that new chemical bonds are formed between our samples and the functional groups of –OH, H⁺, and H₂O molecules in the electrolyte, suggesting that it has a strong absorption capacity of ions and H₂O molecules. In addition, it can be observed for two slight new peaks of 429 and 488 cm⁻¹ under the bias potential of –0.4 V (Supplementary Fig. 46d), corresponding to the ν_{Ni-OH} band of our samples. This result indicates the adsorbed H₂O molecules during the cathodic polarization process are decomposed into H_{ads} species and OH⁻ ions⁶². More importantly, the intensity of these characteristic peaks of 1T_{0.72}-MoS₂@NiS₂ are increased significantly as the potential varies from –0.4 to –1.5 V. It may be due to the OH⁻ being driven to adsorb on Mo, Ni, S atoms in the alkaline medium, and then OOH* intermediates are formed⁶³. As to 1T_{0.81}-MoS₂@Ni₂P sample, we also obtained similar results (Supplementary Fig. 46e, f). We used in situ growth of NiS₂ (or Ni₂P) nanoparticles on the entire surface of 1T-2H MoS₂ microspheres to construct multi-heterojunction interface, which may generate Ni–Mo metal bonds, thereby increasing the number of effective active sites of the catalyst. Due to the introduction of Ni atoms, there is a strong interaction between Ni and Mo atoms on the surface of the catalyst, thereby increasing the local electronic state of Mo atoms, reducing the hydrogen-adsorption energy of the H⁺ on Mo atoms, and thus improving its intrinsic catalytic activity.

X-ray absorption spectroscopy. To investigate electronic states of catalysts, X-ray absorption near-edge structure (XANES) spectra were measured on the fresh catalysts and those after being used in the HER process at three representative potentials (–0.04, –0.1, and –0.2 V), near the onset potential and the overpotential at the current densities of 5 and 10 mA cm⁻² (for 1T_{0.81}-MoS₂@Ni₂P sample), respectively. Figure 5a presents Ni *K*-edge XANES spectra of 1T_{0.81}-MoS₂@Ni₂P catalyst recorded at different applied potentials and reference spectra of Ni foil, NiO, and NiO₂. From the fresh catalyst to that under the –0.04 V potential condition, the absorption edge is shifted to the lower energy side by ~0.5 eV, along with a broadening of the white-line peak, meaning a decrease of the Ni oxidation state. Moreover, when cathodic potentials of –0.04 and –0.1 V versus RHE were applied, a further shift of the absorption edge towards lower energy by ~0.2 eV occurs in relation to the case under the –0.04 V potential condition, implying a distinct decrease in the Ni valence state in 1T_{0.81}-MoS₂@Ni₂P during the HER. Notably, all catalyst spectra exhibit white line at 8350.2–8350.9 eV (Supplementary Fig. 47), corresponding to the 1s to 4p electronic transition, indicating Ni–O local coordination similar to NiOOH and Ni oxides⁶⁴. Using the edge positions of NiO and NiO₂ as references, the Ni average valence state is determined as +3.3, +2.2, +1.8, and +2.0 for the fresh and those used at –0.04, –0.1, and –0.2 V, respectively (Supplementary Table 9). Therefore, Ni cations are reduced under working conditions, which is consistent with the Ni 2p XPS results (Supplementary Fig. 28d). In addition, 1T_{0.72}-MoS₂@NiS₂ (Supplementary Fig. 48) and 1T_{0.41}-MoS₂@Ni(OH)₂ (Supplementary Fig. 49) show similar behavior as Ni valency is decreased from +3.6 (fresh) to +2.4 (–0.1 V) and from +2.7 (fresh) to 1.8 (–0.2 V), respectively. In addition, oxidation of Mo from +4 to +6 after catalysis is observed as shown in Fig. 5b. The fresh 1T_{0.81}-MoS₂@Ni₂P exhibit much broader Mo L₃ XANES absorption than those of the Mo standards (MoS₂, MoO₂, and MoO₃), and its lower edge position indicates reduced Mo admixture. In most cases, the broadening of XANES relates to a lack of crystallinity. Interestingly, after the HER reaction, the broad peak is shifted to higher energy and split, indicating 4d_{t_{2g}} and 4d_{e_g} absorption bands of MoO₃⁶⁵ located at 2524 and 2526 eV, respectively. These results indicate the valence states of Mo cations are increased from approximately +4 to a higher oxidation state (+6) under working conditions. Moreover, sulfur does not take part in catalysis as shown in Fig. 5c. All S *K*-edge XANES spectra of catalysts before and after the reaction are similar and agree well with that of MoS₂ standard. P *K*-edge XANES spectra of 1T_{0.81}-MoS₂@Ni₂P and FePO₄ are shown in Fig. 5d. The white line at 2154 eV belongs to PO₄²⁻ associated with hybridized O 2p- P 3p absorption band⁶⁶ whereas the original Ni₂P species appear only as a minor peak at 2146 eV. The peak position and absorption line shape of Ni₂P are close to that of Co₂P indicates the valence state P³⁻⁶⁷. The ratio of Ni₂P to PO₄²⁻ changes with the cathodic potential, and the highest ratio is 1:3 at –0.2 V. As to the fresh catalyst, the front peak is much weaker, which indicates that although there is a Ni–P bond, its signal is changed by the presence of some other elements. When cathodic potentials of –0.1 and –0.2 V versus RHE were applied, showing the highest intensity of the front peak, which indicates that both P and Ni are involved in the reaction during the HER process.

Overall, the XANES spectra studies provide clear evidence that the structures of as-prepared catalysts can drastically change under realistic catalytic conditions. The Ni site at the interface of heterojunction is most susceptible to low-valence induced by chemisorbed OH⁻ under electrochemical conditions. While the valence state of the Mo site at the interface increases, suggesting that the charge transfer (electron transfer from the Mo site to the

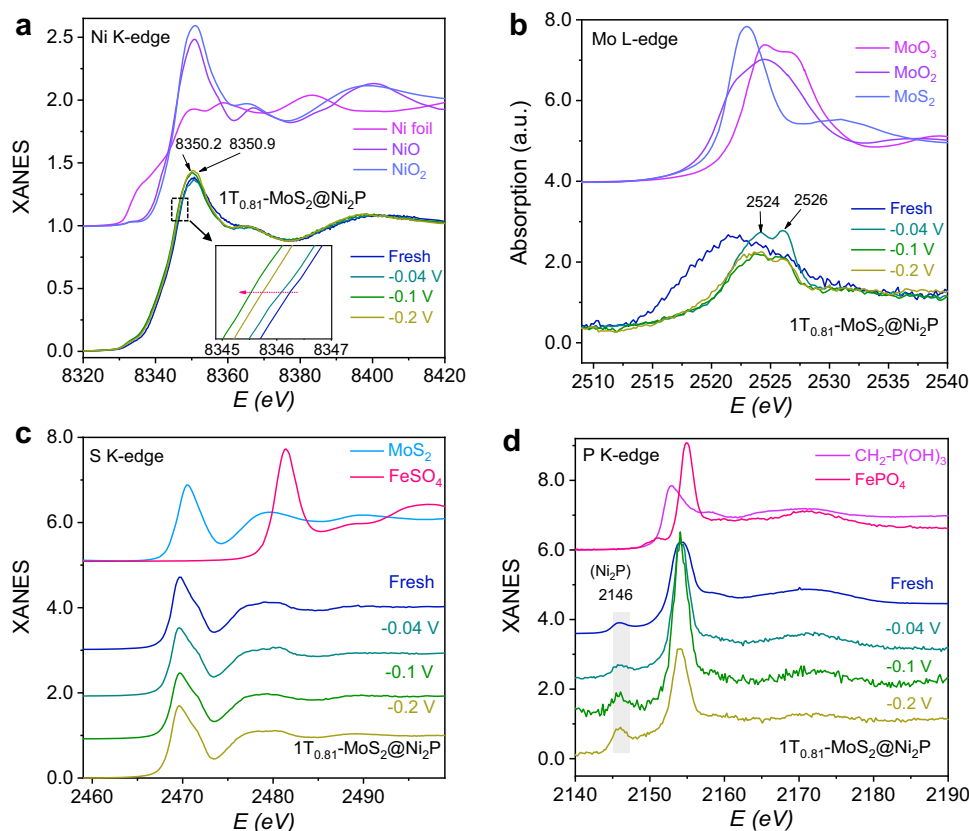


Fig. 5 XANES spectra measurements of fresh $1T_{0.81}\text{-MoS}_2\text{@Ni}_2\text{P}$ catalyst and after being used in the HER process at -0.04 , -0.1 , and -0.2 V vs RHE, respectively. **a** Ni K-edge XANES spectra of $1T_{0.81}\text{-MoS}_2\text{@Ni}_2\text{P}$ catalyst and standards Ni foil, NiO, and NiO₂. Inset, Magnified pre-edge XANES region. **b** Mo L-edge XANES spectra of $1T_{0.81}\text{-MoS}_2\text{@Ni}_2\text{P}$ catalyst and standards MoS₂, MoO₂, and MoO₃. **c** S K-edge XANES spectra of $1T_{0.81}\text{-MoS}_2\text{@Ni}_2\text{P}$ catalyst and standards MoS₂, and FeSO₄. **d** P K-edge XANES spectra of $1T_{0.81}\text{-MoS}_2\text{@Ni}_2\text{P}$ catalyst and standards CH₂-P(OH)₃, and FeSO₄.

Ni site) on the surface of the heterojunction catalyst is accelerated during the HER reaction. Therefore, reduced nickel possesses empty *d*-orbitals, which is beneficial to additional H binding ability. Moreover, it can decrease Mo–H bond strength, and so greatly enhance the HER catalytic activity of as-prepared catalysts.

Discussion

In summary, we have constructed multi-heterogeneous-interface catalysts ($1T_{0.81}\text{-MoS}_2\text{@Ni}_2\text{P}$ and $1T_{0.72}\text{-MoS}_2\text{@NiS}_2$) by tuning its electronic structure of phase modulation synergistic with interfacial chemistry and defects to phosphorus or sulfur implantation strategies, which is an efficient approach to obtain abundant reactive sites of long-cycling and stable electrocatalysts for HER in alkaline and acidic surroundings. The as-achieved $1T_{0.81}\text{-MoS}_2\text{@Ni}_2\text{P}$ and $1T_{0.72}\text{-MoS}_2\text{@NiS}_2$ electrodes only require small overpotentials of 38.9 (or 186) and 98.5 (or 128) mV to drive HER at 10 mA/cm² and have low Tafel slopes: 41 (or 79) and 42 (or 68) mV/dec in 0.5 M H₂SO₄ (or 1.0 M KOH). Accordingly, these results show varieties of multi-heterogeneous interfaces in $1T_{0.81}\text{-MoS}_2\text{@Ni}_2\text{P}$ and $1T_{0.72}\text{-MoS}_2\text{@NiS}_2$ electrodes, which can be considered versatile electroactive sites and facilitate electron transfer because of their unique heterogeneous effects. DFT calculation results also display that the introduction of metallic-phase MoS₂ and intrinsic HER-active Ni-based materials can regulate MoS₂ electronic structure effectively for making the bandgap narrower. In situ electrochemical-Raman spectroscopy indicates that the OH[−] ions are driven to be adsorbed on Mo, Ni atoms in the alkaline medium, and then there form the OOH* intermediates. There is a strong interaction

between Ni and Mo on the surface of the catalyst, thereby increasing the local electronic state of Mo atoms, reducing the hydrogen-adsorption energy for protons on Mo atoms, and thus improving its intrinsic catalytic. Additionally, XANES spectroscopy results imply that reduced Ni supply empty *d*-orbitals to facilitate H atom capture, and decrease Mo–H strength of $1T_{0.81}\text{-MoS}_2\text{@Ni}_2\text{P}$ (or $1T_{0.72}\text{-MoS}_2\text{@NiS}_2$) catalysts that account for the outstanding HER properties with lower Tafel slopes and overpotentials compared with $2H_{\text{phase}}\text{-MoS}_2$, $1T_{\text{phase}}\text{-MoS}_2$ counterparts and other Mo-based catalysts. Thus, our work provides a new horizon for rationally designing multi-heterogeneous interfaces of non-precious electrocatalysts to realize excellent HER activities.

Methods

Synthesis of $1T_{0.41}\text{-MoS}_2$. MoS₂ microspheres were grown on carbon cloth (CC) hydrothermally. First, a CC (2 × 4 cm) was cleaned (for 15 min) using acetone and then sonicated in deionized water and ethanol for 10 min. Then, sodium molybdate (Na₂MoO₄·2H₂O, 411.9 mg) and thiourea (CS(NH₂)₂, 608.96 mg) were added to deionized water (40 mL) and citric acid (20 mL). The mixture was magnetically stirred to form a cleaning solution, then placed into a 100 mL Teflon-lined autoclave and held in it at 180 °C for 12 h. Finally, the CC substrates with $1T_{0.41}\text{-MoS}_2$ microspheres (denoted through the paper as $1T_{0.41}\text{-MoS}_2$) were rinsed using deionized water and ethanol and vacuum-dried for 6 h at 60 °C. For comparison, deionized water was used as the solvent, and $2H_{\text{phase}}\text{-MoS}_2$ microspheres were synthesized hydrothermally at 220 °C for 24 h from the same precursors.

Synthesis of $1T_{\text{phase}}\text{-MoS}_2$. We used Li-intercalated bulk MoS₂ to prepare $1T_{\text{phase}}\text{-MoS}_2$ ⁶⁸. In an Ar-filled glove box, bulk MoS₂ (1.0 g) prepared by stripping were dispersed in 15 mL of 2 M *n*-BuLi/hexane solution and stirred at ambient conditions for 48 h. The resulting black materials were repeatedly rinsed with anhydrous *n*-hexane and then centrifuged to eliminate *n*-butyl lithium excess and other solution impurities. The $1T_{\text{phase}}\text{-MoS}_2$ powder was prepared and was then coated

on the CC substrate. In order to promote better contact between $1T_{\text{phase}}\text{-MoS}_2$ and CC substrate, we annealed (500 °C) the CC loaded with $1T_{\text{phase}}\text{-MoS}_2$ sample under the protection of Ar gas.

Synthesis of $1T_{0.41}\text{-MoS}_2\text{@Ni(OH)}_2$. We use a standard three-electrode system to prepare $1T_{0.41}\text{-MoS}_2\text{@Ni(OH)}_2$. $1T_{0.41}\text{-MoS}_2$ acted as a working electrode, while Pt sheet and Ag/AgCl/3.5 M KCl acted as counter and reference electrodes. Ni(OH)_2 was electrodeposited on the $1T_{0.41}\text{-MoS}_2$ using 0.1 M $\text{Ni(NO}_3)_2$ at 5.0 mA/cm² cathode current density applied for 300 s. $1T_{0.41}\text{-MoS}_2\text{@Ni(OH)}_2$ samples were rinsed with deionized water and ethanol several times and vacuum-dried at 60 °C.

Synthesis of $1T_{0.72}\text{-MoS}_2\text{@NiS}_2$. The $1T_{0.72}\text{-MoS}_2\text{@NiS}_2$ multi-heterogeneous interfaces were prepared by the solid-vapor reaction method. First, a piece of $1T_{0.41}\text{-MoS}_2\text{@Ni(OH)}_2$ grew on CC was put into the quartz tube with 32.0 mg S powder and was then sealed. Secondly, the quartz tube was positioned inside a tube furnace and was calcinated at 500 °C for 60 min to obtain a $1T_{0.72}\text{-MoS}_2\text{@NiS}_2$ electrode.

Synthesis of $1T_{0.81}\text{-MoS}_2\text{@Ni}_2\text{P}$. Similarly, the $1T_{0.81}\text{-MoS}_2\text{@Ni}_2\text{P}$ multi-heterogeneous interfaces were also obtained by the solid-vapor reaction method. First, a piece of $1T_{0.41}\text{-MoS}_2\text{@Ni(OH)}_2$ grew on CC was put into the quartz tube with 31.0 mg red phosphorus and was then sealed. Secondly, the quartz tube was also calcinated at 580 °C for 1.0 h to prepare the $1T_{0.81}\text{-MoS}_2\text{@Ni}_2\text{P}$ electrode. Additionally, 20 wt% Pt/C was also coated on CC substrate (2.0 mg/cm²) and was labeled as 20% Pt/C for comparison.

Materials characterization. All as-synthesized electrodes were characterized by XRD (performed by Bruker D8 Advance instrument) and Raman spectroscopy (performed using Horiba LabRAB HR800 instrument). The sample morphologies were studied using SEM performed by Hitachi SU8010 instrument and TEM (performed by FEI Tecnai F30 instrument). XPS spectra were collected by the ESCALAB 250Xi instrument manufactured by ThermoFisher using Al K α radiation.

Electrochemical measurements. All electrochemical measurements were performed with a CHI 660E Electrochemical Workstation (CHI Instruments, Shanghai Chenhua Instrument Corp., China). The HER performance of different catalysts (1.0 cm²) was characterized using a three-electrode electrochemical cell in N₂-saturated 1.0 M KOH and 0.5 M H₂SO₄ electrolyte, respectively. Before testing the polarization curve, we first perform cyclic voltammetry (CV) for more than 20 cycles to activate the as-prepared catalysts with a scan rate of 50 mV/s. The EIS tests were measured by AC impedance spectroscopy at the frequency ranges 10⁶ to 1.0 Hz at 300 mV. According to the Nernst equation ($E_{\text{RHE}} = E_{\text{Hg/HgO}} + 0.059 \text{ pH} + 0.098$), where E_{RHE} was the potential vs. a reversible hydrogen potential, $E_{\text{Hg/HgO}}$ was the potential vs. Hg/HgO electrode, and pH was the pH value of electrolyte. The electrochemical stability was evaluated by chronoamperometry measurements at a static overpotential, during which the current variation with time was recorded. The ECSA values were measured through CV in the selected non-faradaic range. The current densities have a linear relationship against different scan rates (10–60 mV/s) and the values of the slope were considered as twice of C_{dl} . The Faraday efficiency of the as-fabricated electrodes was determined by the water drainage method, which can be found in Supplementary Note 2 in Supplementary Information for details. The OER tests were performed in O₂-saturated 1.0 M KOH solution, and the others are the same as HER test conditions. The overall-water splitting performance was characterized in 1.0 M KOH using a two-electrode configuration, and the polarization curve was recorded at a scan rate of 5 mV/s. In order to better compare, Pt/C and IrO₂ ink were also synthesized by placing 8 mg Pt/C and 8 mg IrO₂ powder in the mixture of 700 μL ethanol, 300 μL deionized water, and 50 μL Nafion followed by ultrasonication for 30 min, respectively. Then the as-obtained ink was coated onto the carbon cloth (CC) with the loading mass density of about 3.0 mg/cm² and was then dried at 60 °C. The long-term stability measurements were carried out using the chronoamperometry measurements. All polarization curves at 5 mV/s were corrected without iR-compensation.

DFT theoretical calculation

Model building. According to the HRTEM micrographs, $1T_{\text{phase}}\text{-MoS}_2$, $2H_{\text{phase}}\text{-MoS}_2$, Ni₂P, and NiS₂ formed a multiphase heterojunction. $1T_{\text{phase}}\text{-MoS}_2\text{@Ni}_2\text{P}$ interface, $1T_{\text{phase}}\text{-MoS}_2\text{@NiS}_2$ interface, $2H_{\text{phase}}\text{-MoS}_2\text{@Ni}_2\text{P}$ interface, $2H_{\text{phase}}\text{-MoS}_2\text{@NiS}_2$ interface, bulk $1T_{\text{phase}}\text{-MoS}_2$, $2H_{\text{phase}}\text{-MoS}_2$ were also constructed as comparisons. Considering the Van der Waals forces between the two phases, the unrelaxed heterojunction interface distance was set to 3.0 Å. These original structures were obtained from Materials Project Database⁶⁹.

Computational parameters. DFT calculation was applied to calculate electronic structures of two crystal structures by the partial augmented plane-wave method (PAW) implemented in the VASP⁷⁰ using VASPKit code for post-processing. Considering the heterojunction structure, the long-range force correction was

considered by using the DFT-D3 correction method of Grimme⁷¹. The Perdew–Burke–Ernzerhof (PBE) generalized gradient approximation⁷² was implemented for exchange–correlation energy calculations using 550 eV kinetic energy cut off for the plane-wave basis. Then structural optimizations using a conjugate gradient (CG) method based on the pre-optimized structure were repeated until the maximum force component on each atom remained below 0.01 eV/Å. Monkhorst-Pack k-point meshes in the first Brillouin zone of the primitive cell were used the VASPKit code recommended accuracy levels of 0.04 for the optimization calculation and 0.02 for the static calculation, respectively. After fully relaxing the structures, one final (electronic scf) step with the tetrahedron method using Blöchl corrections and denser k-meshes was employed for DOS calculation. In addition to the H adsorbed energy calculations, the frequency calculation of free H and free-energy correction at 298.15 K (including the entropy and zero-point energy contributions) were also calculated. To avoid abnormal entropy contribution, frequencies < 50 cm⁻¹ are set to be 50 cm⁻¹.

XANES spectra measurements. The Mo L₃-edge, P, S, and Ni K-edge XANES spectra were measured at the BL8 beamline of Synchrotron Light Research Institute (SLRI), Thailand⁷³. The SLRI storage ring was operated at 1.2 GeV with an electron current of 80–150 mA. The incident X-ray beam was monochromatized with a double-crystal monochromator equipped with InSb (111) and Ge (220) crystals. XANES measurements were carried out in air at Ni K-edge and under He atmosphere at the lower edges on as-prepared catalysts embedded on carbon cloth and those used as the working electrode in electrochemical reaction with 1 M KOH solution. Cathode voltages from -0.04 V to -0.2 V vs. RHE ($E_{\text{RHE}} = E_{\text{Ag/AgCl}} + 0.059 \text{ pH} + 0.197$) were applied for 160 s using an electrochemical workstation (Autolab PGSTAT204) before the XANES experiment. All XANES spectra were collected in fluorescence-yield mode using a 13-element Si drift detector. Ni and foils, and elemental S and P were used for photon energy calibration. The edge position was defined as the point corresponding to the maximum value in the derivative curves of the XANES spectra. Data normalization was carried out using the Athena software⁷⁴.

Data availability

The authors declare that the main data supporting the findings of this study are available within the article and its Supplementary Information. Extra data are available from the corresponding author upon request.

Received: 11 March 2021; Accepted: 23 August 2021;

Published online: 06 September 2021

References

- Choi, W. et al. High-detectivity multilayer MoS₂ phototransistors with spectral response from ultraviolet to infrared. *Adv. Mater.* **24**, 5832–5836 (2012).
- Shi, J. et al. Two-dimensional metallic tantalum disulfide as a hydrogen evolution catalyst. *Nat. Commun.* **8**, 958 (2017).
- Yang, L. et al. Combining photocatalytic hydrogen generation and capsule storage in graphene based sandwich structures. *Nat. Commun.* **8**, 16049 (2017).
- Yi, J. et al. Large-scale production of ultrathin carbon nitride-based photocatalysts for high-yield hydrogen evolution. *Appl. Catal. B Environ.* **281**, 119475 (2021).
- Wei, Z. et al. Simultaneous realization of sulfur-rich surface and amorphous nanocluster of NiS_{1+x} cocatalyst for efficient photocatalytic H₂ evolution. *Appl. Catal. B Environ.* **280**, 119455 (2021).
- Peng, L. et al. Accelerated alkaline hydrogen evolution on M(OH)_x/M-MoPO_x (M = Ni, Co, Fe, Mn) electrocatalysts by coupling water dissociation and hydrogen ad-desorption steps. *Chem. Sci.* **11**, 2487–2493 (2020).
- Wang, P. et al. Precise tuning in platinum-nickel/nickel sulfide interface nanowires for synergistic hydrogen evolution catalysis. *Nat. Commun.* **8**, 14580 (2017).
- Chen, Y. et al. Electrocatalytically inactive SnS₂ promotes water adsorption/dissociation on molybdenum dichalcogenides for accelerated alkaline hydrogen evolution. *Nano Energy* **64**, 103918 (2019).
- Mahmood, N. et al. Electrocatalysts for hydrogen evolution in alkaline electrolytes: mechanisms, challenges, and prospective solutions. *Adv. Sci.* **5**, 1700464 (2018).
- Sun, Y. et al. Strongly coupled dual zervalent nonmetal doped nickel phosphide nanoparticles/nitrogen, boron-graphene hybrid for pH-universal hydrogen evolution catalysis. *Appl. Catal. B Environ.* **278**, 119284 (2020).
- Seh, Z. W. et al. Combining theory and experiment in electrocatalysis: insights into materials design. *Science* **355**, 1–12 (2017).
- Morales-Guio, C. G. et al. Nanostructured hydrotreating catalysts for electrochemical hydrogen evolution[J]. *Chem. Soc. Rev.* **43**, 6555–6569 (2014).

13. Walter, M. et al. Solar water splitting cells. *Chem. Rev.* **110**, 6446 (2010).
14. Yang, B. et al. Amorphous phosphatized ruthenium-iron bimetallic nanoclusters with Pt-like activity for hydrogen evolution reaction. *Appl. Catal. B Environ.* **283**, 119583 (2021).
15. Gao, B. et al. 3D flower-like defected MoS₂ magnetron-sputtered on candle soot for enhanced hydrogen evolution reaction. *Appl. Catal. B Environ.* **263**, 117750 (2020).
16. Ren, J. et al. Molybdenum-based nanoparticles (Mo₂C, MoP and MoS₂) coupled heteroatoms-doped carbon nanosheets for efficient hydrogen evolution reaction. *Appl. Catal. B Environ.* **263**, 118352 (2020).
17. Yao, N. et al. Oxygen-vacancy-induced CeO₂/Co₄N heterostructures toward enhanced pH-Universal hydrogen evolution reactions. *Appl. Catal. B Environ.* **277**, 119282 (2020).
18. Fan, H. et al. Plasma-heteroatom-doped Ni-V-Fe trimetallic phospho-nitride as high-performance bifunctional electrocatalyst. *Appl. Catal. B Environ.* **268**, 118440 (2020).
19. Wang, H. et al. Confined growth of pyridinic N-Mo₂C sites on MXenes for hydrogen evolution. *J. Mater. Chem. A* **8**, 7109–7116 (2020).
20. Zhang, X. et al. Structure and phase regulation in MoC (α -MoC_{1-x}/β-Mo₂C) to enhance hydrogen evolution. *Appl. Catal. B Environ.* **247**, 78–85 (2019).
21. Ge, Y. et al. Transforming nickel hydroxide into 3D prussian blue analogue array to obtain Ni₂P/Fe₃P for efficient hydrogen evolution reaction. *Adv. Energy Mater.* **8**, 1800484 (2018).
22. Xu, K. et al. Yin-Yang harmony: metal and nonmetal dual-doping boosts electrocatalytic activity for alkaline hydrogen evolution. *ACS Energy Lett.* **3**, 2750–2756 (2018).
23. Anjum, M. A. R. et al. Efficient hydrogen evolution reaction catalysis in alkaline media by all-in-one MoS₂ with multifunctional active sites. *Adv. Mater.* **30**, 1707105 (2018).
24. Chang, K. et al. Targeted synthesis of 2H- and 1T-phase MoS₂ monolayers for catalytic hydrogen evolution. *Adv. Mater.* **28**, 10033–10041 (2016).
25. Kim, M. et al. Covalent 0D–2D heterostructuring of Co₉S₈–MoS₂ for enhanced hydrogen evolution in all pH electrolytes. *Adv. Funct. Mater.* **30**, 2002536 (2020).
26. Kibsgaard, K. et al. Engineering the surface structure of MoS₂ to preferentially expose active edge sites for electrocatalysis[J]. *Nat. Mater.* **11**, 963–969 (2012).
27. Sun, T. et al. Engineering the electronic structure of MoS₂ nanorods by N and Mn dopants for ultra-efficient hydrogen production[J]. *ACS Catal.* **8**, 7585–7592 (2018).
28. Zhang, H. et al. Surface modulation of hierarchical MoS₂ nanosheets by Ni single atoms for enhanced electrocatalytic hydrogen evolution[J]. *Adv. Funct. Mater.* **28**, 1807086 (2018).
29. Liu, Z. et al. Vertical nanosheet array of 1T phase MoS₂ for efficient and stable hydrogen evolution. *Appl. Catal. B Environ.* **246**, 296–302 (2019).
30. Lei, C. et al. Efficient alkaline hydrogen evolution on atomically dispersed Ni–N_x Species anchored porous carbon with embedded Ni nanoparticles by accelerating water dissociation kinetics. *Energy Environ. Sci.* **12**, 149–156 (2019).
31. Wang, S. et al. Ultrastable In-Plane 1T–2H MoS₂ heterostructures for enhanced hydrogen evolution reaction. *Adv. Energy Mater.* **8**, 1801345 (2018).
32. Deng, S. et al. Synergistic doping and intercalation: realizing deep phase modulation on MoS₂ arrays for high-efficiency hydrogen evolution reaction. *Angew. Chem.* **58**, 16289–16296 (2019).
33. Chen, W. et al. Achieving rich and active alkaline hydrogen evolution heterostructures via interface engineering on 2D 1T-MoS₂ quantum sheets. *Adv. Funct. Mater.* **30**, 2000551 (2020).
34. Luo, Y. et al. Morphology and surface chemistry engineering toward pH-universal catalysts for hydrogen evolution at high current density. *Nat. Commun.* **10**, 269 (2019).
35. Zhang, B. et al. Interface engineering: the Ni(OH)₂/MoS₂ heterostructure for highly efficient alkaline hydrogen evolution. *Nano Energy* **37**, 74–80 (2017).
36. Cheng, Y. et al. Defects enhance the electrocatalytic hydrogen evolution properties of MoS₂-based materials[J]. *Chem. Asian J.* **15**, 3123–3134 (2020).
37. Kim, M. et al. Activating MoS₂ basal plane with Ni₂P nanoparticles for Pt-Like hydrogen evolution reaction in acidic media. *Adv. Funct. Mater.* **29**, 1809151 (2019).
38. Lin, J. et al. Defect-rich heterogeneous MoS₂/NiS₂ nanosheets electrocatalysts for efficient overall water splitting. *Adv. Sci.* **6**, 1900246 (2019).
39. Jia, Y. et al. A heterostructure coupling of exfoliated Ni–Fe hydroxide nanosheet and defective graphene as a bifunctional electrocatalyst for overall water splitting. *Adv. Mater.* **29**, 1700017 (2017).
40. Liu, Y. et al. Interface engineering of (Ni, Fe)S₂@ MoS₂ heterostructures for synergistic electrochemical water splitting. *Appl. Catal. B Environ.* **247**, 107–114 (2019).
41. Liu, Z. et al. Heterogeneous nanostructure based on 1T-phase MoS₂ for enhanced electrocatalytic hydrogen evolution. *ACS Appl. Mater. Inter.* **9**, 25291–25297 (2017).
42. Ding, W. et al. Highly ambient-stable 1T-MoS₂ and 1T-WS₂ by hydrothermal synthesis under high magnetic fields. *ACS Nano* **13**, 1694–1702 (2019).
43. Wang, X. et al. 2D/2D 1T-MoS₂/Ti₃C₂ MXene heterostructure with excellent supercapacitor performance. *Adv. Funct. Mater.* **30**, 0190302 (2020).
44. Zheng, X. L. et al. Building a lateral/vertical 1T-2H MoS₂/Au heterostructure for enhanced photo-electrocatalysis and surface enhanced Raman scattering [J]. *J. Mater. Chem. A* **7**, 19922 (2019).
45. Sun, X. et al. Interface engineering in two-dimensional heterostructures: towards an advanced catalyst for ullmann couplings[J]. *Angew. Chem. Int. Ed.* **55**, 1704–1709 (2016).
46. Guo, S. H. et al. Enhanced hydrogen evolution via interlaced Ni₃S₂/MoS₂ heterojunction photocatalysts with efficient interfacial contact and broadband absorption[J]. *J. Alloy. Compd.* **749**, 473e480 (2018).
47. Yu, Y. F. et al. High phase-purity 1T'-MoS₂- and 1T'-MoSe₂-layered crystals[J]. *Nat. Chem.* **10**, 638–643 (2018).
48. Zeng, L. Y. et al. Multiple modulations of pyrite nickel sulfides via metal heteroatom doping engineering for boosting alkaline and neutral hydrogen evolution[J]. *J. Mater. Chem. A* **7**, 25628 (2019).
49. Zeng, L. et al. Three-dimensional-networked Ni₂P/Ni₃S₂ hetero-nanoflake arrays for highly enhanced electrochemical overall-water-splitting activity[J]. *Nano Energy* **51**, 26–36 (2018).
50. Zeng, L. et al. Multiple modulation of hierarchical NiS₂ nanosheets by Mn heteroatom doping engineering for boosting alkaline and neutral hydrogen evolution[J]. *J. Mater. Chem. A* **7**, 25628 (2019).
51. Feng, J. X. et al. Efficient hydrogen evolution on Cu nanodots-decorated Ni₃S₂ nanotubes by optimizing atomic hydrogen adsorption and desorption[J]. *J. Am. Chem. Soc.* **140**, 610–617 (2017).
52. Zhang, J. et al. Synergistic interlayer and defect engineering in VS₂ nanosheets toward efficient electrocatalytic hydrogen evolution reaction. *Small* **14**, 1703098 (2018).
53. Benck, J. D. et al. Amorphous molybdenum sulfide catalysts for electrochemical hydrogen production: insights into the origin of their catalytic activity. *ACS Catal.* **2**, 1916–1923 (2012).
54. Deng, J. et al. Enhanced electron penetration through an ultrathin graphene layer for highly efficient catalysis of the hydrogen evolution reaction. *Angew. Chem. Int. Ed.* **54**, 2100–2104 (2015).
55. Jiao, Y. et al. Porous plate-like MoP assembly as an efficient pH-universal hydrogen evolution electrocatalyst. *ACS Appl. Mater. Inter.* **12**, 49596–49606 (2020).
56. Mishra, I. K. et al. Hierarchical CoP/Ni₂P₄/CoP microsheet arrays as a robust pH-universal electrocatalyst for efficient hydrogen generation. *Energy Environ. Sci.* **11**, 2246–2252 (2018).
57. Li, H. et al. Activating and optimizing MoS₂ basal planes for hydrogen evolution through the formation of strained sulphur vacancies. *Nat. Mater.* **15**, 48–53 (2016).
58. Zhang, B. et al. Simultaneous interfacial chemistry and inner Helmholtz plane regulation for superior alkaline hydrogen evolution. *Energy Environ. Sci.* **13**, 3007–3013 (2020).
59. Zhang, J. et al. Engineering water dissociation sites in MoS₂ nanosheets for accelerated electrocatalytic hydrogen production. *Energy Environ. Sci.* **9**, 2789–2793 (2016).
60. Wu, Y. et al. Electron density modulation of NiCo₂S₄ nanowires by nitrogen incorporation for highly efficient hydrogen evolution catalysis. *Nat. Commun.* **9**, 1425 (2018).
61. Li, Z. et al. Effects of structural changes on the enhanced hydrogen evolution reaction for Pd NPs@2H-MoS₂ studied by in-situ raman spectroscopy[J]. *Chem. Phys. Lett.* **764**, 138267 (2020).
62. Zuleta, A. et al. Improvement of the erosion-corrosion resistance of magnesium by electroless Ni-P/Ni(OH)₂-ceramic nanoparticle composite coatings[J]. *Surf. Coat. Technol.* **304**, 167–178 (2016).
63. Zhang, S. et al. In situ interfacial engineering of nickel tungsten carbide janus structures for highly efficient overall water splitting[J]. *Sci. Bull.* **65**, 640–650 (2020).
64. Chung, Y.-H. et al. Anomalous in situ activation of carbon-supported Ni₂P nanoparticles for oxygen evolving electrocatalysis in alkaline media. *Sci. Rep.* **7**, 8236 (2017).
65. Tsai, H.-M. et al. Anisotropic electronic structure in quasi-one-dimensional K_{0.3}MoO₃: an angle-dependent x-ray absorption study. *Appl. Phys. Lett.* **91**, 022109 (2007).
66. Prietzel, J. et al. Reference spectra of important adsorbed organic and inorganic phosphate binding forms for soil P speciation using synchrotron-based K-edge XANES spectroscopy. *J. Synchrotron Rad.* **23**, 532–544 (2016).
67. Zhang, Y. et al. Structural designs and in-situ X-ray characterizations of metal phosphides for electrocatalysis. *Chem. Cat. Chem.* **12**, 3621–3628 (2020).
68. Luo, Y. et al. Two-dimensional MoS₂ confined Co(OH)₂ electrocatalysts for hydrogen evolution in alkaline electrolytes. *ACS Nano* **12**, 4565–4573 (2018).
69. Jong, M. et al. Charting the complete elastic properties of inorganic crystalline compounds. *Sci. Data.* **2**, 150009 (2015).

70. Intan, N. et al. Ab initio modeling of transition metal dissolution from the $\text{LiNi}_{0.5}\text{Mn}_{1.5}\text{O}_4$ cathode. *ACS Appl. Mater. Inter.* **11**, 20110–20116 (2019).
71. Grimme, S. et al. Effect of the damping function in dispersion corrected density functional theory. *J. Comput. Chem.* **32**, 1456–1465 (2011).
72. Perdew, J. et al. Generalized gradient approximation made simple. *Phys. Rev. Lett.* **78**, 1396–1396 (1997).
73. Klysubun, W. et al. Upgrade of SLRI BL8 beamline for XAFS spectroscopy in a photon energy range of 1 keV to 13 keV. *Radiat. Phys. Chem.* **175**, 108145 (2020).
74. Ravel, B. et al. Hephaestus: data analysis for X-ray absorption spectroscopy using IFEFFIT. *J. Synchrotron Rad.* **12**, 537–541 (2005).

Acknowledgements

We thank Dr. Yuting Luo, Feng-Ning Yang, Zhiyuan Zhang, and Jun-Rong Zeng for the helpful discussions. This work was supported by the Science Foundation of the National Key Laboratory of Science and Technology on Advanced Composites in Special Environments (Grant No. 6142905192507), Shenzhen Science and Technology Plan Supported Project (Grant No. JCYJ20170413105844696), China Scholarship Council (Grant No. 201606125092), the National Key R&D Project from Minister of Science and Technology in China (No. 2016YFA0202701), the University of Chinese Academy of Sciences (Grant No. Y8540XX2D2), the National Natural Science Foundation of China (No. 52072041), External Cooperation Program of BIC, Chinese Academy of Sciences (No. 121411KYS820150028), the 2015 Annual Beijing Talents Fund (No. 2015000021223ZK32), and Qingdao National Laboratory for Marine Science and Technology (No. 2017ASKJ01). XANES experiment was supported by Synchrotron Light Research Institute (SLRI), Suranaree University of Technology (SUT), and Thailand Science Research and Innovation (TSRI). Dr. Wipada Senanon and BL8 staffs are acknowledged for their assistances.

Author contributions

M.L. and J.W. contributed equally to this work. G.-G.W. and Y.Y. supervised the project. M.L. designed, performed, and analyzed the experiments and devised the heterogeneous-interface catalysts; J.W. conducted theoretical calculation section; W.K. and S.S. performed XANES spectra measurements; W.K. revised XANES interpretation; F.L., Y.C., F.Z., and J.Y. discussed the results and helped the preparation of figures, which were

revised by Y.Y. The manuscript was written by M.L., and revised by J.W., G.-G.W., and Y.Y.

Competing interests

The authors declare no competing interests.

Additional information

Supplementary information The online version contains supplementary material available at <https://doi.org/10.1038/s41467-021-25647-8>.

Correspondence and requests for materials should be addressed to G.-G.W. or Y.Y.

Peer review information *Nature Communications* thanks Lijun Gao, Alberto Vomiero and the other, anonymous, reviewer(s) for their contribution to the peer review of this work. Peer reviewer reports are available.

Reprints and permission information is available at <http://www.nature.com/reprints>

Publisher's note Springer Nature remains neutral with regard to jurisdictional claims in published maps and institutional affiliations.



Open Access This article is licensed under a Creative Commons Attribution 4.0 International License, which permits use, sharing, adaptation, distribution and reproduction in any medium or format, as long as you give appropriate credit to the original author(s) and the source, provide a link to the Creative Commons license, and indicate if changes were made. The images or other third party material in this article are included in the article's Creative Commons license, unless indicated otherwise in a credit line to the material. If material is not included in the article's Creative Commons license and your intended use is not permitted by statutory regulation or exceeds the permitted use, you will need to obtain permission directly from the copyright holder. To view a copy of this license, visit <http://creativecommons.org/licenses/by/4.0/>.

© The Author(s) 2021